Sādhanā Vol. 40, Part 4, June 2015, pp. 1313–1341. © Indian Academy of Sciences

Numerical assessment of non-uniform corrosion scenarios of rebar in concrete exposed to natural chloride environment

S MUTHULINGAM[1] and B N RAO[2,*]

[1]Department of Civil Engineering, SSN College of Engineering, Kalavakkam 603 110, India
[2]Structural Engineering Division, Department of Civil Engineering, Indian Institute of Technology Madras, Chennai 600 036, India
e-mail: bnrao@iitm.ac.in

MS received 18 July 2014; revised 18 October 2014; accepted 21 January 2015

Abstract. Corrosion of embedded rebars is a classical deterioration mechanism that remains as one of the most significant problems limiting the service life of concrete structures exposed to chloride-laden environments. The primary objective of this study is to propose and verify a numerical framework that can efficiently quantify non-uniform corrosion penetration depth along the perimeter of the rebar in concrete exposed to chloride environment. This framework investigates the corrosion process during both the corrosion initiation and propagation phases by exploring the effects of not only the rebar existence but also its sizes and locations. The corrosion initiation phase is examined through a comprehensive chloride ingress model that identifies the most important parameters that influence the intrusion of chlorides into RC. The corrosion propagation phase is studied based on a decisive parameter, namely, the corrosion rate. In addition, the framework evaluates the non-uniform corrosion states that correspond to two scenarios of corrosion penetration depth: corrosion of segment of the rebar and uneven corrosion along the rebar perimeter. Numerical solution shows that, in general, chloride build-up along the perimeter of the corner bar is not only faster but also higher than that of the middle bar. Moreover, for the given values of cover thickness and water-to-binder ratio, time-to-corrosion initiation for the corner bar is faster than that for the middle bar. Furthermore, the larger the rebar, in general, the bigger the obstruction, and therefore, the higher the chloride build-up. Qualitative comparisons of the evaluated non-uniform corrosion scenarios with the variety of available laboratory and field data show good agreement.

Keywords. Corrosion; steel reinforced concrete; chloride ingress; corrosion rate; finite element modeling.

*For correspondence

1. Introduction

The total service life of reinforced concrete (RC) components subject to chloride-induced corrosion is generally represented as a two stage process consisting of an initiation phase and a propagation phase (Tuutti 1982; Weyers 1998). Corrosion initiation phase refers to the depassivation process of rebar by the presence of chloride ions and involves the coupled transport processes of chloride, moisture and heat through the porous concrete cover (Saetta *et al* 1993; Martin-Perez *et al* 2001). An alkaline passive layer (pH $\sim$ 13–14) around the steel and a thick concrete cover, acting as a barrier against the intrusion of aggressive species, provide chemical and physical protection to the embedded rebar, respectively. Nevertheless, steel depassivation occurs when the concentration of chloride at the rebar level reaches a critical chloride content thereby destroying the passive layer. Critical chloride content for RC is the amount of chloride at the depth of the rebar necessary to sustain localized breakdown of its passive film and hence initiate its active corrosion (Schiessl & Raupach 1990). The time taken by chloride ions from external environments to reach the critical value at the rebar depth is defined as time-to-corrosion initiation (TCI).

The process of chloride ingress into concrete is very complex for the following three reasons: (1) interaction between many physical and chemical phenomena; (2) dependence on many internal parameters (level of hydration in concrete, porosity, binder type, etc); and (3) external environmental conditions (temperature, relative humidity, chloride, etc). Therefore, various models have been developed, from analytical models based on Fick's second law of diffusion to highly sophisticated mathematical models taking the mechanisms of chloride ingress process into account. The complex process of chloride ingress into concrete is commonly simplified as a diffusion problem and the same is represented through the mathematical expression proposed by Fick in (1855). The Gauss error function based analytical solutions to Fick's law are also widely reported in the literature for limited initial and boundary conditions. However, these analytical solutions are valid only under the following conditions: (1) concrete is homogeneous; (2) weak temperature gradients in concrete; (3) concrete remains fully saturated and not subjected to any water movement; (4) constant chloride diffusion coefficient in time and space; and (5) concrete surfaces subject to a constant chloride exposure (Song *et al* 2008; Marchand & Samson 2009). As an alternative to Fick's law, researchers (e.g. Saetta *et al* 1993; Iqbal and Ishida 2009) proposed physics based mathematical models with various levels of complexity for enhanced modelling of chloride ingress into concrete. These mathematical models incorporate detailed transport equations and provide more reliable service life predictions.

The existence of rebar is of greater importance with respect to chloride ingress into RC, mainly because: (1) length of the corrosion initiation phase is determined in large part by the rate at which the chloride builds adjacent to the rebar; and (2) higher accumulation of chlorides around the steel-to-concrete interfaces of larger-size bars results in faster corrosion (Kranc *et al* 2002; Oh & Jang 2003; Muthulingam & Rao 2014). However, in many studies based on mathematical models, the rebar in concrete is either modeled as a fully insulated region or neglected in the numerical analysis (e.g. Martin-Perez *et al* 2001; Bastidas-Arteaga *et al* 2011; Shafei *et al* 2012). Although rebars are impermeable to intrusions by moisture and chlorides, they can transport heat much faster than the surrounding concrete because of their higher thermal conductivity. Furthermore, the numerical algorithm of Saetta *et al* (1993) has a general applicability for understanding the process of chloride ingress into concrete under various environmental exposure conditions (e.g. Martin-Perez *et al* 2001; Kong *et al* 2002). This numerical algorithm; (1) incorporates

the dependence of chloride diffusion coefficient on the material parameters of concrete, internal relative humidity and temperature; and (2) considers the effects of nonlinear chloride binding. Nevertheless, the numerical algorithm of Saetta *et al* (1993) has not yet been exploited to examine the effect of not only the existence of rebar but also its size and location on the process of chloride ingress into RC. Therefore, it is highly desirable that such a numerical algorithm be enhanced by incorporating the existence of rebars. Most recently, Muthulingam & Rao (2014) presented a detailed parametric study on TCI of rebars and explored qualitatively the effects of various factors, such as critical chloride content, structural configuration and distance from the coastline, by limiting diffusion as the dominant mode of chloride transport.

Corrosion propagation phase refers to the mechanical degradation process of RC structures under corrosion attack and involves much more complex procedures such as the formation of electrochemical corrosion cells (microcell and macrocell), reduction in the cross-sectional area of rebar, rust expansion induced concrete cover cracking, spalling and delamination (Bhargava *et al* 2011). In recent years, greater emphasis has been placed on investigating the corrosion propagation phase (Liu & Weyers 1998; Weyers 1998; Kong *et al* 2002; Li *et al* 2006; Yuan *et al* 2007; Val *et al* 2009; Bhargava *et al* 2011). This allows for the realistic estimation of various damage parameters such as time-to-cover cracking, crack width and cover spalling (DuraCrete 1998). However, vast majority of models (Liu & Weyers 1998; Kong *et al* 2002; Li *et al* 2006; Yuan *et al* 2007; Val *et al* 2009; Bhargava *et al* 2011) developed assume a uniform corrosion penetration depth along the entire perimeter of the rebar, which is contrary to field observations (e.g. Liu & Li 2004). Owing to the spatially and temporally evolving chloride ion content through concrete cover thickness and to the impermeable nature of steel bars, rebar may not be corroding uniformly along its entire perimeter.

The rebar surfaces facing the external environment, where chloride accumulations are faster and higher, begin to corrode first. In a rectangular or square RC cross-section, such surface regions for corner bars are around the midpoints of quadrants facing the adjacent concrete cover surfaces and for middle bars are around shortest distances from respective concrete cover surfaces. Whereas, over the steel surfaces facing the interior of concrete, amount of chloride ions remain at a very low-level because of the impermeable nature of steel bars. Hence, breakdown of passive protection layer and corrosion of steel could hardly happen in this region before the cracking of concrete cover. Thus, variations in the onset of corrosion reaction along the perimeter of the rebar lead to non-uniform corrosion states. Non-uniform corrosion states correspond to corrosion scenarios where only a region of the rebar perimeter is corroding and where corrosion is occurring unevenly along the perimeter of the rebar. The importance of considering the real state of corrosion in rebar is also supported by the fact that the effect of non-uniform corrosion induced stresses in RC is more conducive to cover cracking than uniform corrosion (Kim & Kim 2008; Xia *et al* 2012).

The primary objective of this study is to propose and verify a numerical framework that can efficiently quantify non-uniform corrosion penetration depth along the perimeter of the rebar in concrete exposed to chloride environment. This framework considers the effects of rebar size and location on the process of chloride ingress into concrete and evaluates the non-uniform corrosion states that correspond to two scenarios of corrosion penetration depth: corrosion of segment of the rebar and uneven corrosion along the rebar perimeter. The corrosion initiation phase is examined through a comprehensive chloride ingress model that identifies the most important parameters (both external and internal) influencing the intrusion of chlorides into RC. The environmental parameters, namely, ambient temperature, relative humidity and chloride content are

categorized as external parameters, while the concrete properties and diffusion characteristics are considered as internal parameters. The corrosion propagation phase is studied based on a decisive parameter, namely, the corrosion rate which depends on various factors, such as concrete resistivity, concrete quality, cover depth, temperature, humidity and chloride content. However, this framework does not account for the effects of concrete cracking that can increase both concrete diffusivity and corrosion rate during the corrosion propagation phase (Djerbi *et al* 2008; Otieno *et al* 2010).

2. Chloride ingress model

Depending on the environmental exposure conditions of RC, corrosion initiation phase is characterized by simultaneous yet different operations of chloride ingress mechanisms such as diffusion and convection (e.g. Iqbal & Ishida 2009; Shafei *et al.* 2012). Diffusion is the main transport process in the case of water-saturated concrete, e.g. submerged RC components. Convection is usually the dominant mechanism for concrete in the splash zone, for instance, seawater or salt bearing water on roads (Meira *et al* 2010). The problem of chloride ingress into concrete can effectively be studied as the interaction between three phenomena, namely: heat transport; moisture transport; and chloride transport. Each of these phenomena is represented by a partial differential equation (PDE) and their interaction is considered by solving them simultaneously. The governing PDEs representing the process of chloride ingress into concrete can be expressed in the following general form:

$$\Upsilon \dot{\Phi} + \underbrace{\vec{\nabla} \cdot \left(\Theta \vec{\nabla} \Phi\right)}_{\text{diffusion}} + \underbrace{\vec{\nabla} \cdot \left(\Psi \, \Phi \, \vec{\nabla} \Gamma\right)}_{\text{convection}} = 0. \tag{1}$$

The correspondence between Υ, Θ, Φ, Ψ, Γ and the terms for the transport quantity is presented in table 1.

For chloride transport, C_f is the free chlorides content dissolved in the pore solution (kg/m^3), D_c^a and D_h^a represent apparent chloride and humidity diffusion coefficients (m^2/s), respectively:

$$D_c^a = \frac{D_{c,ref} \, f_c\,(T) \, f_c\,(t) \, f_c\,(h)}{1 + \frac{1}{w_e}\left(\frac{\partial C_b}{\partial C_f}\right)}, \tag{2}$$

$$D_h^a = \frac{D_{h,ref} \, f_h\,(T) \, f_h\,(h) \, f_h\,(t_e)}{1 + \frac{1}{w_e}\left(\frac{\partial C_b}{\partial C_f}\right)}, \tag{3}$$

Table 1. Correspondence between Eq. 1 and the governing field equations.

Transport quantity	Diffusion terms			Convection terms	
	Φ	Υ	Θ	ψ	Γ
Chloride	C_f	1	D_c^a	D_h^a	h
Moisture	h	$\frac{\partial w_e}{\partial h}$	D_h	–	–
Heat	T	ρc_p	D_T	–	–

where $D_{c,ref}$ and $D_{h,ref}$ are reference chloride and humidity diffusion coefficients (m^2/s) measured under standard conditions ($T = 23°C$, $t_e = 28$ days, $h = 100\%$) (Saetta *et al* 1993), w_e is evaporable water content (m^3 of water/m^3 of concrete), f_c and f_h are modification factors to account for the effects of temperature, relative humidity (h, a ratio between water vapor pressure and saturated vapor pressure), ageing, and the level of hydration in concrete. These factors are detailed in Muthulingam & Rao (2014). The term $\partial C_b/\partial C_f$ represents the binding capacity of the cementitious system which is the slope of either Langmuir or Freundlich binding isotherm (Muthulingam & Rao 2014). The binding isotherm relates the free and bound chloride content at equilibrium and is characteristic of each cementitious system (Tang & Nilsson 1993). Further, it needs to be clarified here that the chloride transport is based on single-ion approach that considers only chloride ions transport. Alternatively, multi-ionic approaches have also been developed that take into account the intricate interaction between different ions and the hydrated cement paste during chloride ingress into concrete (Samson & Marchand 2007; Baroghel-Bouny *et al* 2011). Although, multi-ionic approaches can be used to better model the process of chloride ingress into concrete, would require a larger number of input parameters, and these data are not always readily available or easy to obtain (Marchand & Samson 2009; Papakonstantinou & Shinozuka 2013). Hence, in the current study, a single-ion approach based model that incorporates nonlinear chloride binding relationships, humidity and temperature variations is used to model the process of chloride ingress into concrete.

For moisture transport, D_h represents humidity diffusion coefficient (m^2/s) and the derivative of water content with respect to pore relative humidity (i.e. $\partial w_e/\partial h$) is defined as moisture capacity. It needs to be noted here that different transport mechanisms, such as convection, diffusion, desorption, adsorption, and capillary suction may apply individually or simultaneously for the transport of water in the concrete. Although one or more of the mentioned transport mechanisms may become dominant depending on the pore relative humidity and micro-structure of the concrete, Walton *et al* in 1990 (cited in Shafei *et al* 2012) indicated that the diffusion process usually dominates the transport of moisture in the concrete. At standard temperature and pressure, adsorption isotherm relates evaporable water content and pore relative humidity. Based on thermodynamic principle of adsorption, Braunauer-Skalny-Bodor model considers this relationship to depend on temperature, water-to-binder ratio (a ratio by mass) and level of hydration in concrete, t_e (days) (Xi *et al* 1994). From the adsorption isotherm, moisture capacity can be obtained by taking its derivative with respect to h:

$$\frac{\partial w_e}{\partial h} = \frac{CkV_m\left(Ch^2k^2 - h^2k^2 + 1\right)}{(hk-1)^2\,(Chk - hk + 1)^2}, \tag{4}$$

where C is a constant that takes into account the influence of change in temperature on the adsorption isotherm, k is a constant resulted from the assumption that the number of adsorbed layers is a finite small number and V_m represents the monolayer capacity (equal to the mass of adsorbate required to cover the adsorbent with a single molecular layer). These parameters are detailed in Muthulingam & Rao (2014).

The penetration of chloride ions occurs mostly through the pore structure of the concrete or the concrete micro cracks caused by drying shrinkage or temperature changes (Bertolini 2008). Moreover, ambient temperature is one of the external parameters that directly affect the diffusion process in the concrete (Shafei *et al* 2012). Further, temperature, relative humidity, and cement hydration evolution cause variability of chloride diffusion coefficient in both time and space (Saetta *et al* 1993). Therefore, amongst other parameters such as concrete porosity, cement type,

and curing conditions, temperature is one of the important parameters that have significant effect on the rate of chloride penetration (Detwiler *et al* 1991). For heat transport, ρ is the density of concrete (or) rebar (kg/m^3), c_p is the specific heat capacity of concrete (or) rebar (J/kg K) and D_T is the thermal conductivity of concrete (or) rebar (W/m K). Specific heat of the concrete is generally expressed in terms of thermal capacity, which is a product of specific heat and density. The specific heat capacity of normal strength concrete is affected at temperatures above 600°C by the physicochemical processes that occur in the cement paste and the aggregates (Kodur & Sultan 2003). Below 600°C, the specific heat capacity for normal strength concrete ranges between 840 and 1170 J/kg C (Neville 1963).

Specific heat capacity of the rebar within the temperature range of 20–600°C can be estimated by using the following expression given in Eurocode 3:

$$c_{p,\text{rebar}} = 425 + 7.73 \times 10^{-1} T_r - 1.69 \times 10^{-3} T_r^2 + 2.22 \times 10^{-6} T_r^3 \text{ [J/kg °C]}, \quad (5)$$

where T_r represents rebar temperature (°C). It is widely accepted that thermal conductivity has an influence on the temperature gradient along the concrete. Very specifically the thermal conductivity of normal strength concrete depends on aggregate volume fraction, fine aggregate fraction, water-to-binder ratio, temperature and moisture condition (Kim *et al* 2003):

$$D_{T,\text{concrete}} = D_{T,ref} \left[\begin{array}{c} [0.293 + 1.01 A_g] \left[0.8 \left(1.62 - 1.54 \left(\frac{w}{b} \right) \right) + 0.2h \right] \\ [1.05 - 0.0025T] \left[0.86 + 0.0036 \left(\frac{s}{a} \right) \right] \end{array} \right] \text{[W/m K]}, \quad (6)$$

where s/a is fine aggregate fraction, A_g is aggregate volume fraction, $D_{T,ref}$ is reference thermal conductivity (W/m K), and w/b represents water-to-binder ratio. Even though the thermal conductivity of concrete slightly increases with water content and is affected by temperature, variations are small, and it can be assumed constant (Bazant & Thonguthai 1978). Thermal conductivity of the rebar within the temperature range of 20–800°C can be estimated by adopting the following expression (Eurocode 3):

$$D_{T,\text{rebar}} = 54.0 - 3.33 \times 10^{-2} T_r \text{ [W/m K]}. \quad (7)$$

3. Corrosion rate and corrosion penetration depth

The corrosion rate (i_{corr}) of rebars in concrete structures is one of the most important parameters for making reasonable service life prediction in the corrosion propagation phase (Li *et al* 2006; Otieno *et al* 2012). Corrosion rate of rebars in concrete structures is affected by various factors, namely, supplementary cementitious materials, moisture content, cyclic wetting and drying, sustained loading, loading history, concrete resistivity, concrete quality, cover depth, temperature, cracking, dissolved oxygen content and exposure conditions (Otieno *et al* 2012). By considering few or more of the above-mentioned factors, various corrosion rate prediction models were proposed in the literature. Detailed reviews of the corrosion rate prediction models are given in the literature (Raupach 2006; Otieno *et al* 2012) and will not be discussed here.

Corrosion level of the rebar is generally determined in terms of depth of the attack penetration (e.g. Val *et al* 2009). The corrosion penetration depth, p_d (mm) at an exposure time,

t(years) after corrosion initiation, t_c can be estimated based on Faraday's law (Rodriguez *et al* 1996):

$$p_d(t) = \int_{t_c}^{t} 0.0116\, i_{\text{corr}}(t)\, dt. \tag{8}$$

The time-dependent corrosion penetration depth, $p_d\ (t)$ can be estimated by incorporating various corrosion rate empirical models with Eq. 8. By substituting the DuraCrete (1998) model into Eq. 8 and integrating, $p_d(t)$ becomes

$$p_d\ (t)\ =\ 0.0116\ i_{\text{corr-20}}\,[1 + k_1\ (T\ (t) - 20)]\ (t\ -\ t_c)\,, \tag{9}$$

where $i_{\text{corr-20}}$ is the corrosion rate at 20°C, $k_1\ =\ 0.025$ if $T(t)\ <\ 20$°C and $k_1\ =\ 0.073$ if $T(t)\ >\ 20$°C. Similarly, for the corrosion rate model of Liu & Weyers (1998), $p_d(t)$ can be given as

$$p_d(t) = \int_{t_c}^{t} 0.0116\ \exp\left(\left(\begin{array}{c} 7.89 + 0.7771\ln(1.69C_t) - \dfrac{3006}{T} \\ -0.000116R_c + 2.24\,t^{-0.215} \end{array}\right) - \ln(1.08)\right) dt, \tag{10}$$

where C_t represents total chloride content (TCC) in kg/m^3, R_c is the ohmic resistance of the concrete cover (Ω) and t is the corrosion time (years). R_c can be calculated by another empirical relationship suggested in the literature (Liu 1996):

$$\ln\ R_c = 8.03 - 0.549\ \ln\ (1 + 1.69\,C_t)\ \ [\Omega]. \tag{11}$$

Since it is challenging to evaluate the closed form integral of Eq. 10, a numerical integration is performed by adopting the trapezoidal rule. For the corrosion rate model of Vu & Stewart (2000), $p_d\ (t)$ can be expressed as

$$p_d\ (t) = 0.5249\frac{\left[1 - \left(\dfrac{w}{b}\right)\right]^{-1.64}}{C_c}\ (t\ -\ t_c)^{0.71}\,, \tag{12}$$

where C_c represent concrete cover thickness (cm) and w/b represents water-to-binder ratio. Finally, for the corrosion rate model of Yu *et al* (2014), $p_d\ (t)$ becomes

$$p_d\ (t) = 0.0116\left(c_1 h + \frac{1}{c_2\,h^2\ +\ c_3\,h}\ +\ c_4\right)\ (t\ -\ t_c)\,. \tag{13}$$

The corrosion rate model coefficients of Yu *et al* (2014), namely, c_1, c_2, c_3, and c_4 can be either obtained directly or linearly interpolated from the values reported by the authors. Furthermore, BS 6349-1 suggested the mean and upper limit values of corrosion rate for various exposure zones that apply to each face exposed to the environment of the zone. It may be noted here that the corrosion rate empirical models (Eqs. 9–13) are based on the process of uniform corrosion. In the current study, they are adopted to estimate non-uniform corrosion penetration depth along the perimeter of the rebar. Moreover, as macrocell regions are evolving in time along the perimeters of rebars, passive-to-active zone ratios diminish leading to drastic changes in macrocell corrosion rates. Furthermore, oxygen control is often regarded as the most critical controlling mechanism in the corrosion propagation phase. As steel is normally embedded in sound concrete cover, oxygen diffuses through the porous

concrete cover to reach steel surface in order for the cathodic reaction at both the active zone and the passive zone (Cao & Cheung 2014). In the current study, neither the drastic change in macrocell corrosion rate nor oxygen diffusion is accounted during the corrosion propagation phase. This is a simplification of the problem; a more complete representation of the macrocell corrosion rate could be obtained by solving the governing equations of potential distribution and electrical current flow during the corrosion process.

4. Numerical model

From Section 2, it is evident that the corrosion initiation phase in RC is modeled through a set of three PDEs (see table 1) that describes heat, moisture and chloride transports into concrete. Three PDEs are numerically solved in space as a boundary-value problem and in time as an initial-value problem by means of a 2D finite element (FE) formulation, in which appropriate boundary conditions are enforced to simulate monthly variations in temperature and relative humidity. The evolution of spatial distribution of the different variables with time is integrated by adopting the finite difference method. In this study full-scale FE model is adopted as opposed to concrete cover region truncated models reported in the literature (e.g. Martin-Perez *et al* 2001) mainly to capture the spatial and temporal distributions of TCC and TCI profiles along the perimeters of rebars. FE formulation of the governing PDEs is well documented in the literature (e.g. Martin-Perez *et al* 2001) and will not be dealt here.

4.1 *Boundary and initial conditions*

Pertinent boundary conditions are enforced to simulate seasonal variations in exposure conditions. Time-dependent boundary conditions, considering monthly mean variations of temperature and relative humidity are applied at the exposed boundaries as fluxes. These boundary conditions can be expressed in the following general form:

$$X = \underbrace{\alpha\left(\Phi^b - \beta\right)}_{\text{diffusion}} + \underbrace{\gamma\,\alpha\left(\Phi^b - \beta\right)}_{\text{convection}}. \tag{14}$$

The correspondence between X, α, β, γ and the different boundary conditions associated with the diffusion and convection terms of the transport quantity is presented in table 2.

In table 2, X_c^b is chloride flux at the exposed boundary (kg/m^2 s), X_h^b is relative humidity flux at the exposed boundary (m/s), X_T^b is heat flux at the exposed boundary (W/m^2), B_c is chloride transfer coefficient at the exposed boundary (m/s), B_h is relative humidity transfer coefficient at the exposed boundary (m/s), B_T is heat transfer coefficient at the exposed boundary (W/m^2 K), C^b is chloride content at the exposed boundary (kg/m^3), h^b relative humidity at the exposed

Table 2. Correspondence between Eq. 14 and the imposed boundary conditions.

Transport quantity	X	Diffusion terms			Convection terms			
		Φ^b	α	β	Φ^b	α	β	γ
Chloride	X_c^b	C_f^b	B_c	C_{env}	h^b	B_h	h_{env}	C_{env}
Moisture	X_h^b	h^b	B_h	h_{env}	–	–	–	–
Heat	X_T^b	T^b	B_T	T_{env}	–	–	–	–

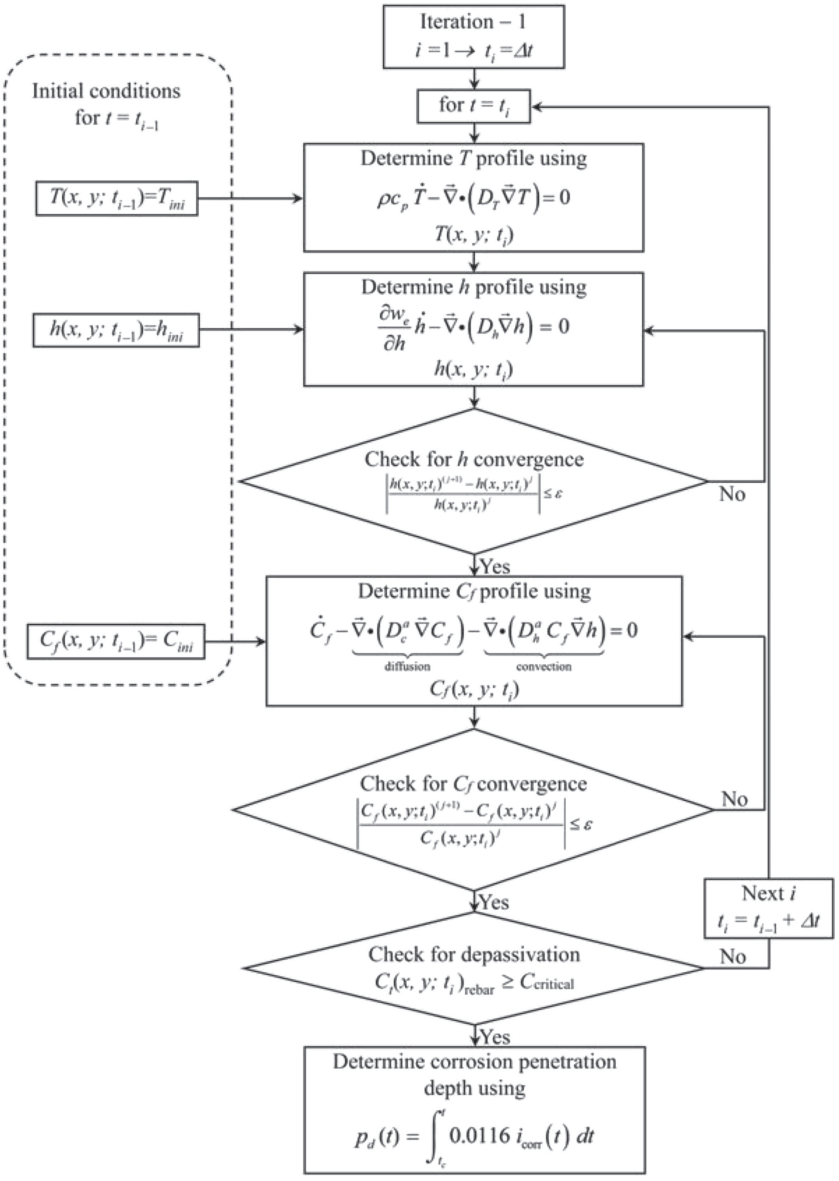

Figure 1. Algorithm for estimating time-dependent temperature, humidity, chloride, and corrosion penetration depth profiles.

boundary, T^b is temperature at the exposed boundary (K), C_{env} is chloride content in the surrounding environment (kg/m^3), h_{env} is relative humidity in the surrounding environment and T_{env} is temperature in the surrounding environment (K). The initial conditions prescribe constant temperature and relative humidity value throughout FE mesh, and their values would depend on the environmental exposure conditions. Concrete mix is assumed to be devoid of any chloride content; consequently, initial chloride is taken as zero for all numerical analysis.

4.2 *Solution procedure*

Figure 1 shows the flowchart for estimating time-dependent variation of the profiles of temperature, humidity, chloride and corrosion penetration depth over the computational domain for 2D simulations. During numerical simulations: (1) heat transport is allowed to take place through rebars; and (2) insulated boundary conditions are enforced along the perimeters of rebars during moisture and chloride transports to account for their impermeable nature. After input of the general geometry of FE mesh, material properties, critical chloride content, and boundary and initial conditions, the solution proceeds as follows:

(a) Corrosion initiation phase

a.1. Determine actual temperature profile throughout the FE mesh (including rebar) from Eq. 1 by taking into account the initial temperature profile $T\ (x,\ y;\ t\ =\ t_{i-1})$.

a.2. Determine humidity profile throughout the FE mesh (excluding rebar) from Eq. 1 by taking into account the temperature profile estimated in the previous step and the initial humidity profile $h\ (x,\ y;\ t\ =\ t_{i-1})$.

a.3. Perform iterative procedure to obtain the actual profile of h by using the profile of h obtained from the previous iteration until a given convergence criterion (ε) is reached. This iterative procedure is adopted to account for the nonlinear nature of Eq. 1 for moisture transport, and the dependency of humidity diffusion coefficient D_h and adsorption isotherm on the actual profiles of h.

a.4. Evaluate the amount of evaporable water, $w_e\ (x, y;\ t_i)$ from adsorption isotherm.

a.5. Evaluate free chloride profile throughout the FE mesh (excluding rebar) from Eq. 1 by taking into account the temperature and humidity profiles estimated in the previous step and the initial free chloride profile $C_f\ (x,\ y;\ t\ =\ t_{i-1})$.

a.6. Perform iterative procedure to obtain the actual profile of C_f by using the profile of C_f obtained from the previous iteration until a given convergence criterion (ε) is reached. This iterative procedure is adopted to account for the nonlinear nature of Eq. 1 for chloride transport and the dependency of apparent chloride diffusion coefficient D_c^a on the actual profiles of C_f.

a.7. Determine TCC values, $C_t\ (x, y;\ t_i)$ by using the chloride binding relationship and the adsorption isotherm.

a.8. If TCC values at the level of the rebar have reached the critical value, corrosion is assumed to have initiated. Hence go to step b, otherwise repeat the procedure for the next $i\ (t_i\ =\ t_{i-1}\ +\ \Delta t)$ from step a.1 by using current profiles of T, h and C_f as initial values.

(b) Corrosion propagation phase

b.1. Determine time-dependent corrosion penetration depth $p_d\ (t)$ from Eq. 8 at depassivated region along the perimeter of the rebar.

b.2. Evaluate non-uniform corrosion states of rebar based on the estimated spatial distributions of $p_d\ (t)$.

In order to implement the numerical algorithm as a single multiphysics code, able to solve the PDEs governing different transport phenomena, namely: heat, moisture and chloride transport,

an object-oriented approach is implemented using C language. Unstructured meshes most suit the RC geometry due to the presence of curved boundaries along the perimeter of the rebar. The source code executes two major tasks, namely, element matrix evaluation and its assembly, and solving the system of equations, of which the former is parallelized.

5. Problem statement

The concrete quality (i.e. water-to-binder ratio) and concrete cover thickness influences the time at which chloride reaches a critical value at the level of the rebar (Balabanic *et al* 1996; Oh & Jang 2003). The relationship between reference chloride diffusion coefficient, $D_{c,ref}$ and water-to-binder ratio is considered based on the following expression (Petcherdchoo 2013):

$$D_{c,ref} = 10^{1.776+1.364\ (w/b)} + (5.806 - 18.69\ (w/b))\ f[\text{mm}^2/\text{year}], \tag{15}$$

where f represents the level of fly ash replacement in percentage and w/b is water-to-binder ratio. For illustrating the numerical framework, the study area, namely Tohoku region in Japan is considered. In Japan the wind usually blows from west to east, the RC structures in Tohoku region near the Sea of Japan (East Sea) have suffered most from severe damage due to airborne chlorides (Akiyama *et al* 2010). Moreover, an RC component is assumed to be located near the shoreline of Tohoku; hence, a constant surface chloride content value of 9 kg/m^3 and a critical chloride content value of 1.2 kg/m^3 of TCC reported by Japan Society of Civil Engineers, JSCE (2007) are adopted in the numerical analysis. Furthermore, the mean monthly temperature and relative humidity data of Tohoku region are obtained for the last 15 years (1998–2012) from Japan Meteorological Agency, JMA, to find the annual trend of the temperature and relative humidity. From the database, it is observed that the recorded temperature and relative humidity have a periodic trend over the year and a sinusoidal function (with time t in years) can be fitted to the data:

$$T_{env}\,(t) = 288.9 + 11.15 \sin(2\pi t) \tag{16}$$

$$h_{env}\,(t) = 0.70 + 0.08 \sin(2\pi(t - 0.5))\,. \tag{17}$$

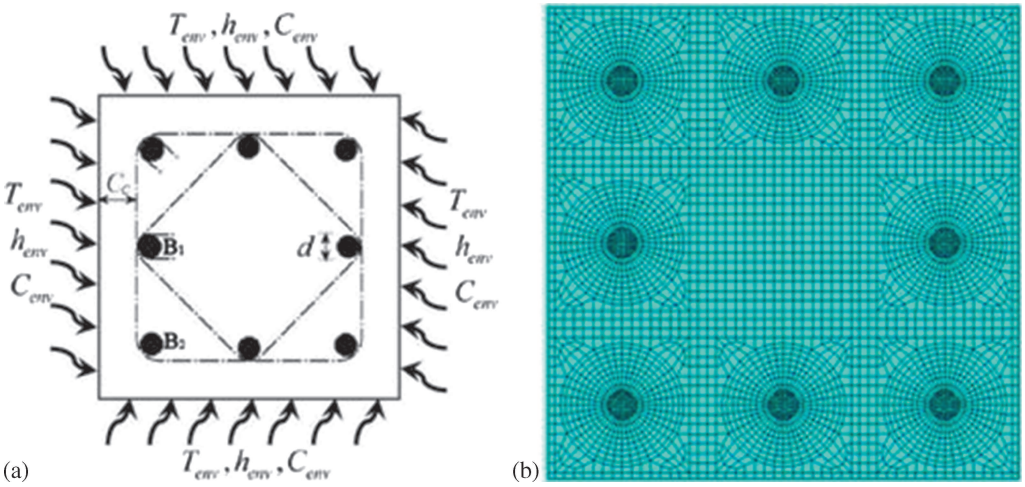

Figure 2. Studied RC component: (**a**) Cross-section and (**b**) Finite element mesh.

For further study an RC component section of size 400 × 400 mm shown in figure 2(a), reported by Pillai & Menon (2009) is considered. In the considered cross-section: (1) C_c and d represent cover thickness and rebar size respectively; and (2) eight rebars are present of which, two bars of interest in future discussions are named B_1 (middle bar) and B_2 (corner bar). To consider the effects of rebar sizes and locations on TCC and TCI, various bar diameters (12, 16, 20, and 25 mm), cover thicknesses (25–75 mm in multiples of 5 mm), and water-to-binder ratios (0.4, 0.5, and 0.6) are considered in this study. The adopted RC cross-section is discretized into four-noded quadrilateral isoparametric elements as shown in figure 2(b). Care is taken to ensure that sufficient number of nodes are present along the perimeter of the rebar (40 nodes) to capture the smooth progress of TCC and TCI. It needs to be noted here that stirrups, being very close to the external environment than the longitudinal bars, are highly susceptible to faster corrosion initiation. However, this work does not account for the presence of stirrups in the concrete cross-section and focuses only on the corrosion of longitudinal rebar. Moreover, to study the effects of corrosion on longitudinal bars and stirrups simultaneously, 3D models would be required, which is not within the scope of the present work.

In FE analysis, all the input values except the material parameter values of concrete and rebar are assumed as indicated in Muthulingam & Rao (2014) except; (1) the thermal conductivity values of concrete and rebar; and (2) specific heat capacity value of the rebar, which are estimated by using Eqs. 5–7. Moreover, DuraCrete (1998) reported value of $i_{\text{corr-20}} = 2.586\ \mu\text{A/cm}^2$ for airborne sea water exposure and BS 6349-1 suggested mean value of $p_d = 0.04$ mm/side/year for atmospheric zone are adopted in the numerical analysis. In addition, the initial values of temperature and relative humidity are assumed as $T_{ini} = 288.9$ K and $h_{ini} = 0.70$, respectively. Furthermore $D_{h,ref}$ values of 1×10^{-12}, 5×10^{-12} and 2.5×10^{-11} m^2/s are considered for the water-to-binder ratios of 0.4, 0.5 and 0.6 respectively (Saetta *et al* 1993). Based on the numerical simulations, the following two sections discuss the effects of rebar locations and sizes on the process of chloride ingress into RC.

6. Results and discussion

6.1 *Effect of rebar location*

This section considers two typical locations of the rebar in an RC component (i.e. middle bar (B_1) and corner bar (B_2) in figure 2(a)) for discussion. Numerical solution shows that, in general, TCC build-up along the perimeter of the corner bar (B_2) is not only faster but also higher than that of the middle bar (B_1). This is because the chloride flow is 2D for the corner bar, whereas it is 1D for the middle bar (see figure 2(a)). In addition, region of the steel surface exposed to the chloride environment for the corner bar is much larger than that for the middle bar.

The effect of rebar location on TCC build-up is demonstrated as follows. For simplicity, only few parameters are used here. Consider a rebar size of 16 mm, six concrete cover thicknesses (30–55 mm in multiples of 5 mm) and three water-to-binder ratios (0.4, 0.5, and 0.6). Figures 3(a)–(f) present the spatial distribution of TCC values along the perimeters of B_1 and B_2 bars after performing a numerical simulation for 50 years by adopting the chloride ingress model described in Section 2.

For the given water-to-binder ratio of 0.4, numerical analysis yields the maximum TCC values of 1.01, 0.71, and 0.47 kg/m^3 for B_1 bar, and 1.54, 1.13, and 0.78 kg/m^3 for B_2 bar having 45, 50, and 55 mm cover thicknesses, respectively. These values imply that, comparing with middle bars, corner bars in general are much more prone to higher TCC build-up along their surfaces. Other combinations of water-to-binder ratio and cover thickness also indicate similar trends in

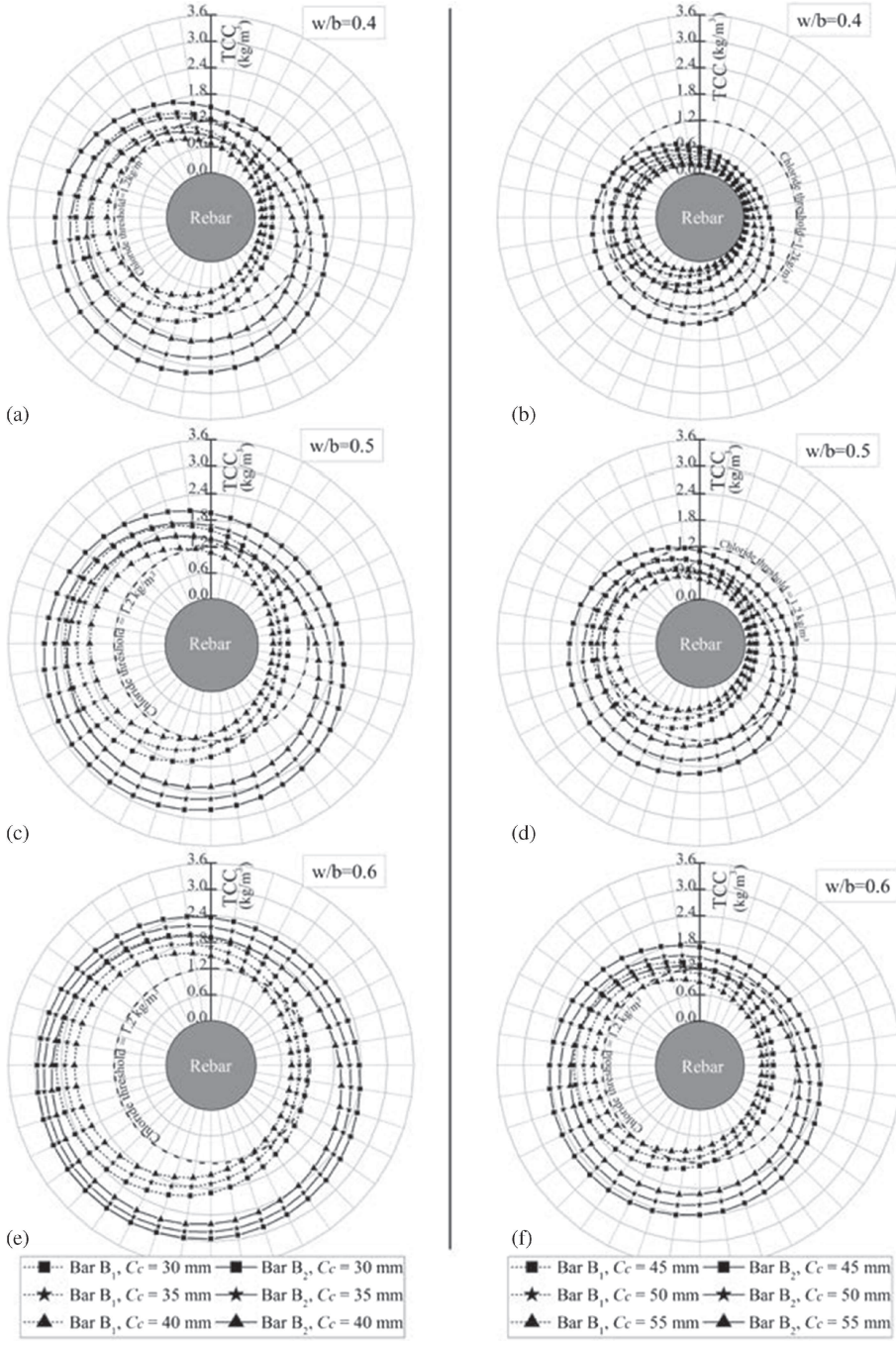

Figure 3. Spatial distribution of TCC values along the perimeter of B_1 and B_2 bars of 16 mm diameter for various combinations of cover thickness (30–55 mm) and water-to-binder ratio (w/b) after 50 years: (**a**,**b**) $w/b = 0.4$, (**c**,**d**) $w/b = 0.5$, and (**e**,**f**) $w/b = 0.6$.

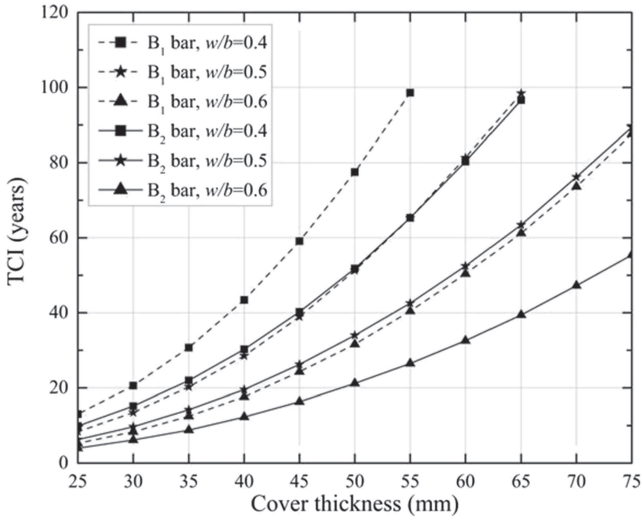

Figure 4. TCI Vs cover thickness for B_1 and B_2 bars of 16 mm diameter.

TCC values between B_1 and B_2 bars. Moreover, figures 3(a)–(f) show that, TCC build-up at the segment of the rebar facing the interior of concrete is much less when compared with that facing the external environment. Even such build-up for B_2 bar appears to be higher than that for B_1 bar.

The effect of rebar location on TCI is examined by considering a rebar of size 16 mm, different water-to-binder ratios (0.4, 0.5 and 0.6) and cover thicknesses (25–75 mm in multiples of 5 mm). Figure 4 illustrates that, for the given values of cover thickness and water-to-binder ratio, TCI for B_2 bar is faster than that for B_1 bar. Additionally, the ratio between TCI of B_1 and B_2 bar falls within the range of 1.3–1.6, indicating TCI for B_2 bar is 30–60% faster than that for B_1 bar. The direct implication of this observation is that the subsequent onset of cracking, as corrosion level increases over time would be much more serious in concrete cover around the corner bars than that in concrete cover around the middle bars. Therefore, corner bars need more protection from external chloride environment. Similar observation in relation to the high corrosion vulnerability of corner bars and the importance of their protection was also reported in the literature (Xia *et al* 2012).

6.2 *Effect of rebar size*

The surfaces of rebars facing the external chloride environment act as obstructions to the penetration of chloride ions into concrete. Due to this phenomenon, chloride ions begin to build-up more on the exposed surfaces of the rebars. The larger the rebar, in general, the bigger the obstruction and therefore, the higher the chloride build-up. Figures 5(a)–(f) demonstrate these facts by illustrating the spatial distribution of TCC values along the perimeters of B_1 and B_2 bars having various sizes (12, 16, 20, and 25 mm) after 25 and 50 years of exposure to chlorides. Figures 5(b) (d), and (f) show that, TCC values at the segments of the rebars facing the external environment increases with the increase in the rebar size for B_1 bar at 25 and 50 years, and for B_2 bar at 50 years. On the contrary, figures 5(a), (c), and (e) exhibit that, such TCC build-up decrease with the increase in the rebar size for B_2 bar at 25 years. These distinctive variations in TCC values over

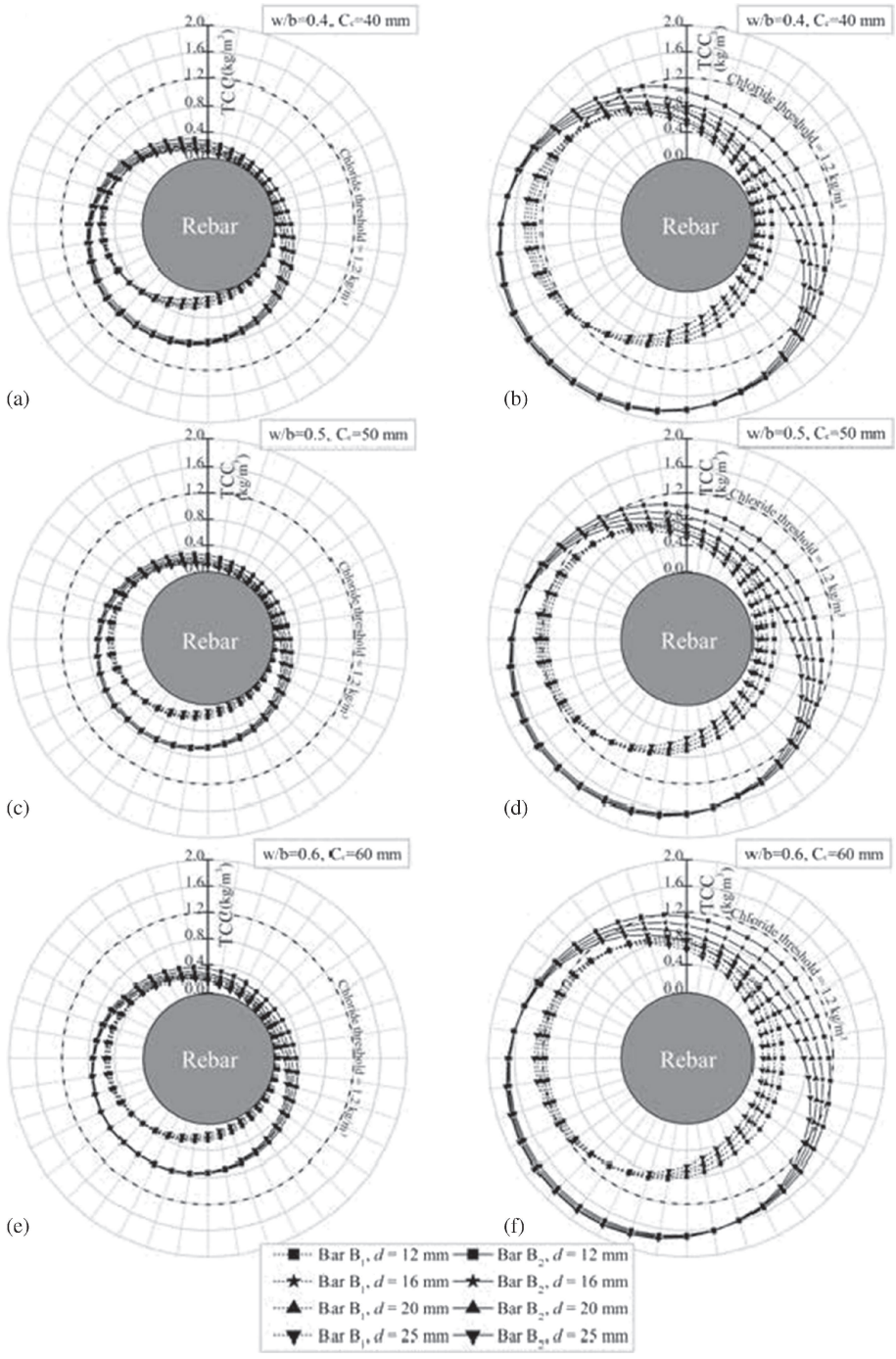

Figure 5. TCC distributions at the surfaces of B_1 and B_2 bars for various combinations of diameter size, cover thickness and water-to-binder ratio (w/b): (**a**) $w/b = 0.4$, $C_c = 40$ mm at 25 years, (**b**) $w/b = 0.4$, $C_c = 40$ mm at 50 years, (**c**) $w/b = 0.5$, $C_c = 50$ mm at 25 years, (**d**) $w/b = 0.5$, $C_c = 50$ mm at 50 years, (**e**) $w/b = 0.6$, $C_c = 60$ mm at 25 years, and (**f**) $w/b = 0.6$, $C_c = 60$ mm at 50 years.

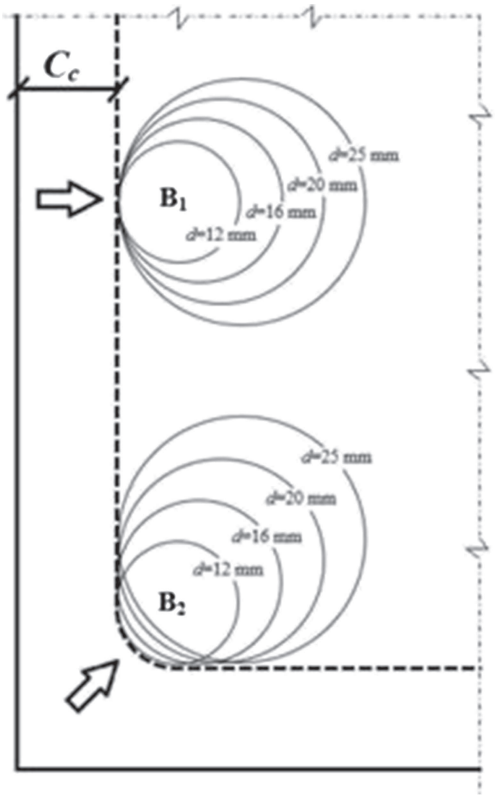

Figure 6. Concrete cross-section along with rebars.

the surfaces of the rebars can be effectively explained by considering the concrete cross-section as shown in figure 6 along with the rebar of various sizes (12, 16, 20, and 25 mm).

In figure 6, arrows identify the specific maximizing penetration paths for B_1 and B_2 bars that signify faster and higher chloride build-up at the segments of the rebars facing the external environment. Figure 6 shows that for a given value of cover thickness, the maximizing penetration path remains constant with the increasing size of B_1 bar, whereas it increases with the increasing size of B_2 bar. These aspects govern the TCC build-up during the shorter exposure periods (say 25 years) and hence with the increase in the rebar size, an increase and decrease in TCC values (figures 5(a), (c), and (e)) are observed for B_1 and B_2 bars. In contrast, during the higher exposure periods (say 50 years), the phenomenon of higher chloride build-up on the exposed surface of the larger-size B_2 bar rather than the increase in maximizing penetration path governs the TCC values (see figures 5(b), (d), and (f)). In other words, with the increase in B_2 bar size, increase in both the maximizing penetration path and the phenomenon of higher chloride build-up take place simultaneously. This significant observation reveals the existence of a transition period for B_2 bar, which is explained below.

The transition period defined in this context is the time during which for the increase in the size of B_2 bar, TCC value at the exposed surface of B_2 bar shifts from being governed by the increase in the maximizing penetration path to being governed by the phenomenon of higher chloride build-up. Figure 7 illustrates the transition in TCC values for the concrete having a cover thickness of 40 mm and various diameter sizes (12, 16, 20, and 25 mm). The transition

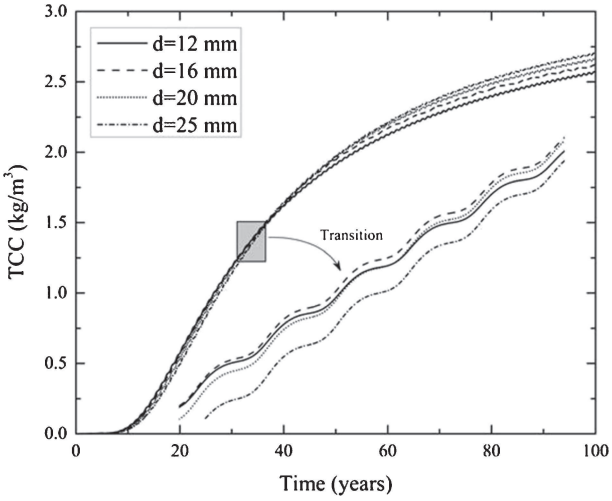

Figure 7. Transition in TCC values for B_2 bars with 40 mm cover thickness.

period varies widely for various parameters (water-to-binder ratio, cover thickness, and rebar size) considered in this study, and it is predicted to range between 30 and 40 years for the specific case under consideration (figures 5(b), (d), and (f)). The transition period has the direct implication in the corrosion initiation process of B_2 bar as will be discussed in detail below.

Large-size rebars proneness to higher chloride build-up lead to faster corrosion. The corrosion reaction sets in first at locations along the perimeters of rebars, where the chloride build-up is faster and higher. In other words, depassivation occurs initially at the surfaces of rebars pointed by the maximizing penetration paths (shown with arrows in figure 6). Thus the penetration paths that maximize the TCC values at the surfaces of rebars minimize TCI values. The effects of rebar size on TCI are illustrated as follows. Consider different sizes of the rebar (12, 16, 20, and 25 mm) along with various combinations of water-to-binder ratio (0.4, 0.5, and 0.6) and cover thickness (25–75 mm in multiples of 5 mm). Figures 8(a) and (b) depict the distribution of TCI values for different combinations of above-mentioned parameters.

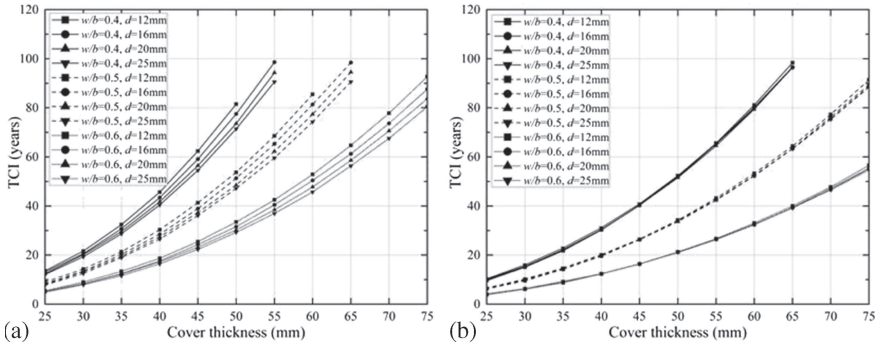

Figure 8. TCI Vs cover thickness for various diameter sizes: (**a**) B_1 bar and (**b**) B_2 bar.

Figure 8(a) shows that, for the given values of cover thickness and water-to-binder ratio, with the increase in the rebar size, TCI for B_1 bar is faster by about 4–6% between any two intermediate sizes (i.e. 12 and 16 mm, 16 and 20 mm, and 20 and 25 mm) and about 10–15% between the extreme sizes (i.e. 12 and 25 mm). However, figure 8(b) illustrates that, for the given values of cover thickness and water-to-binder ratio, with the increase in the rebar size, TCI for B_2 bar before and after the transition period is slower and faster by about 0.2–7% and about 1–4% between both intermediate and extreme sizes, respectively. This behaviour is attributed to the fact that, before the transition period, the maximizing penetration path that minimizes TCI for B_2 bar increases with increase in the rebar size resulting in slower TCI. Whereas, after the transition period, chloride build-up becomes higher with the increase in the size of B_2 bar leading to faster TCI. A noteworthy observation after comparing the effects of increase in the rebar size on TCC and TCI is that, before the transition period, the middle bar (i.e. B_1) has more negative effect (i.e. faster corrosion) than the corner bar (i.e. B_2). However, if the rebar depassivation occurs after the transition period, having a larger-size bar will result in faster TCI irrespective of the rebar location. The significance of this observation is that the sizes of rebar also influence the cracking of concrete cover due to corrosion-induced expansion of rebar. An experimental investigation by Williamson & Clark (2000) also reported that the rebar size influences the failure pressure required to cause cover cracking of concrete.

Concrete cover acts as a barrier against the intrusion of chlorides from the external environment and thus sustains the corrosion-free service life of an RC component. Hence, it is of vital importance to estimate the adequate (minimum) cover thickness for achieving a specified design life of an RC component under aggressive chloride-laden environments. Such plots as figures 8(a) and (b) can be used to determine the minimum cover thickness required to guarantee a certain number of corrosion-free service life to an RC component. For example, table 3 lists the minimum cover thicknesses required to sustain 50 years of corrosion-free service life of an RC component for various rebar locations and water-to-binder ratios. Table 3 illustrates that the minimum cover thickness increases not only with the increase in water-to-binder ratio but also with the rebar location. The former is due to the increase in chloride diffusivity with the increase in water-to-binder ratio, whereas the latter is due to the differences in chloride build-ups. Additionally, table 3 confirms that the sustenance of corrosion-free service life of an RC component under chloride environment is governed by the onset of the corrosion reaction in corner bars rather than middle bars. This is a notable contribution because, traditionally, the cover thickness is considered as an effective parameter to sustain the corrosion-free service life of RC components under aggressive environments; however, the effects of rebar sizes and locations are also significant, and are seldom reported in the literature.

6.3 *Time-to-corrosion initiation profiles*

The results in the preceding two sub-sections demonstrated that the TCC values vary along the perimeters of rebars. This observation leads to the fact that each TCC value at the surface of the rebar will reach a critical chloride value at different exposure periods. Consequently, TCI values

Table 3. Minimum cover thickness for corrosion-free service life of 50 years.

	$w/b = 0.4$		$w/b = 0.5$		$w/b = 0.6$	
Parameters	Bar B_1	Bar B_2	Bar B_1	Bar B_2	Bar B_1	Bar B_2
C_c (mm)	40	45	50	55	60	70

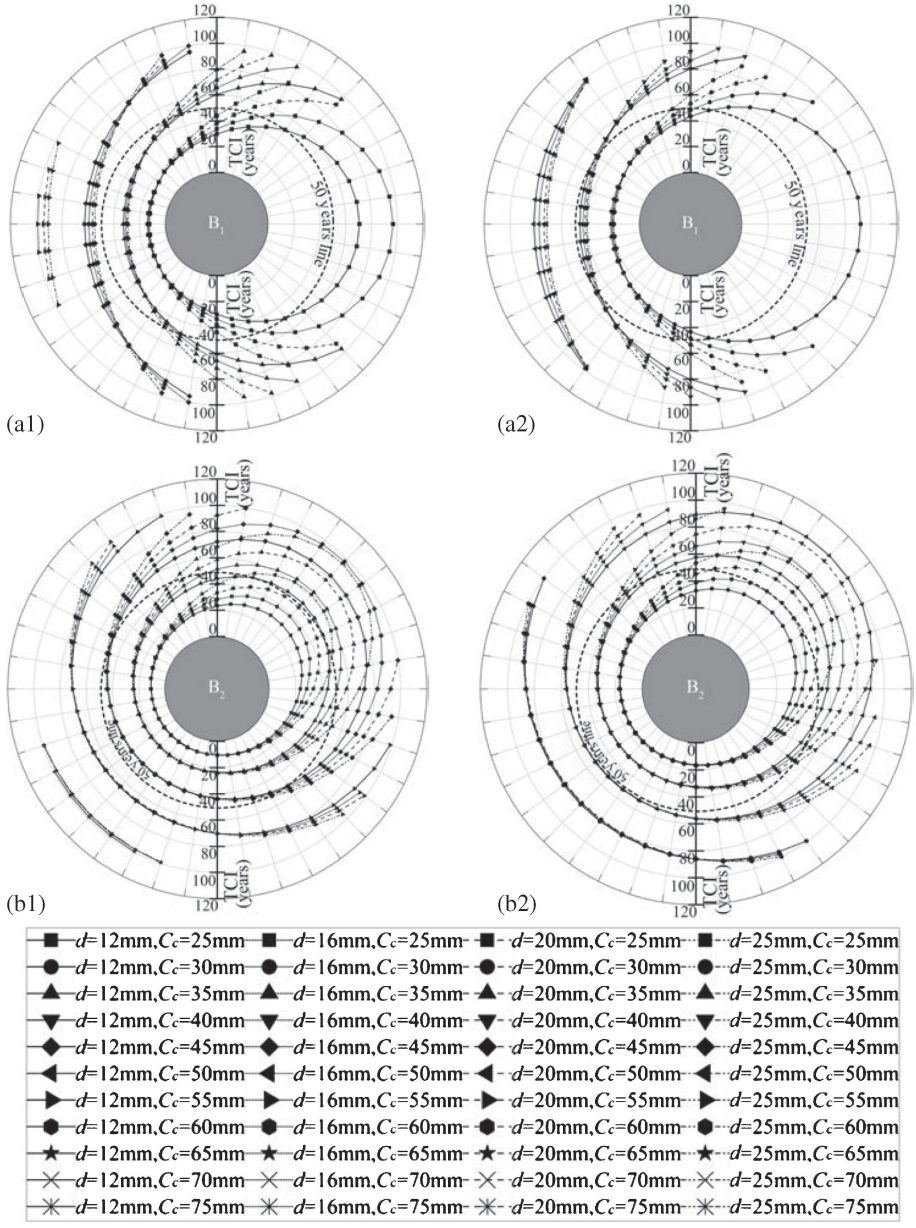

Figure 9. TCI profiles for different combinations of water-to-binder ratio (w/b), rebar diameter size and concrete cover thickness: (**a**) $w/b = 0.4$ and B_1 bar, (**b**) $w/b = 0.4$ and B_2 bar, (**c**) $w/b = 0.5$ and B_1 bar, (**d**) $w/b = 0.5$ and B_2 bar, (**e**) $w/b = 0.6$ and B_1 bar, and (**f**) $w/b = 0.6$ and B_2 bar.

will be both spatially and temporally distributed along the perimeters of rebars, and the same are presented here as TCI profiles. Figures 9(a)–(f) show the TCI profiles corresponding to B_1 (i.e. middle bar) and B_2 (i.e. corner bar) bars for various combinations of water-to-binder ratio (0.4, 0.5, and 0.6), concrete cover thickness (25–75 mm in multiples of 5 mm) and rebar size

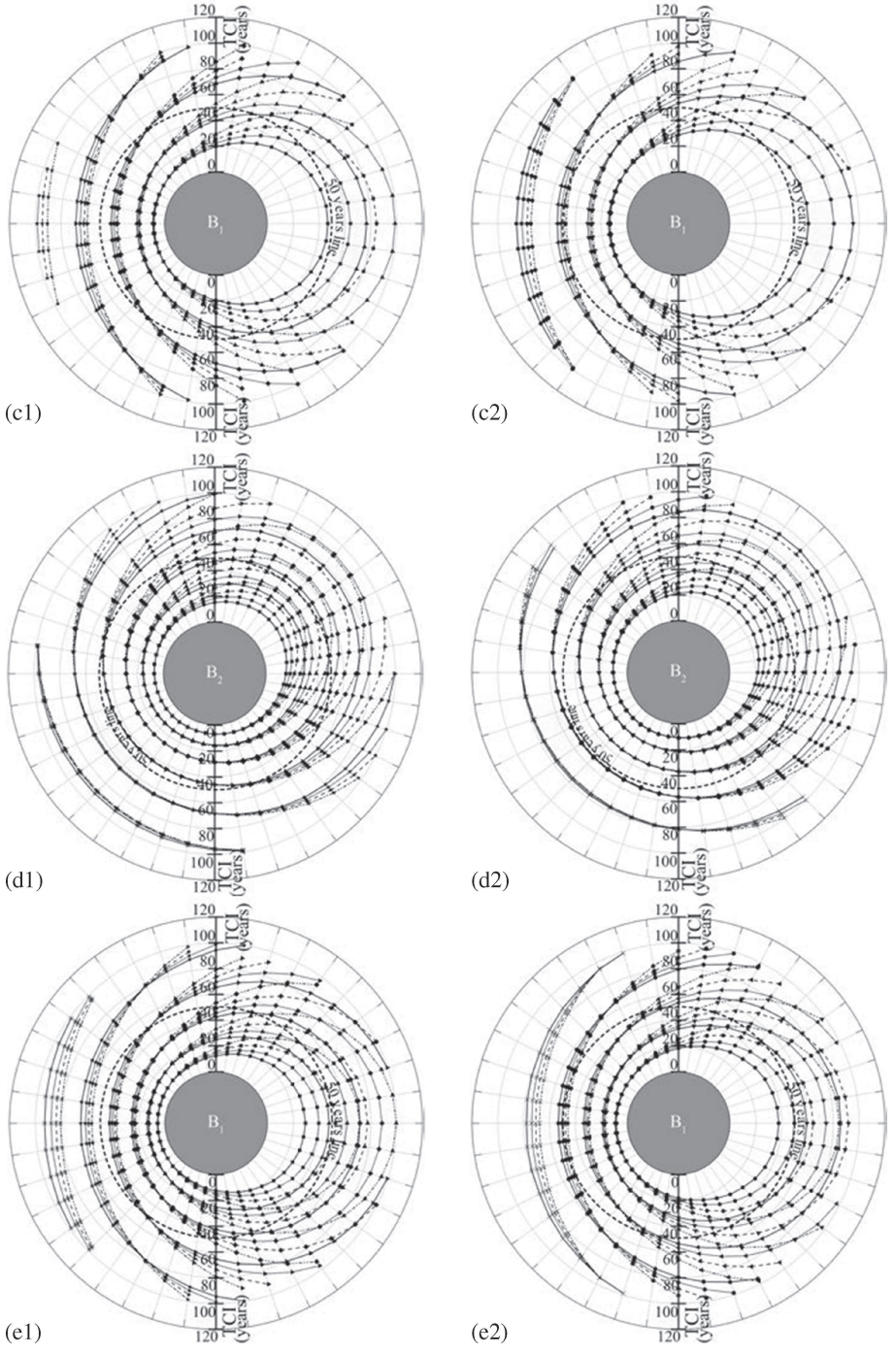

Figure 9. (continued)

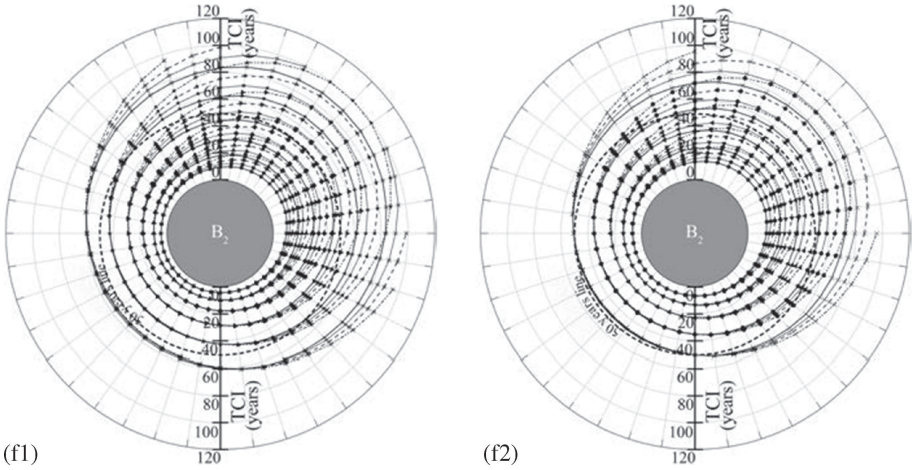

Figure 9. (continued)

(12, 16, 20, and 25 mm). Figures 9(a)–(f) disclose that, even after 100 years of exposure, not all of the combinations of above-mentioned parameters result in complete TCI profile along the perimeters of rebars. A complete TCI profile refers to the distribution of TCI values along the entire perimeter of the rebar. Moreover, from any one of the TCI profile (figures 9(a)–(f)), it is easy to assess the extents of corrosion initiated region along the perimeter of a rebar over time.

TCI profiles in figures 9(a)–(f) show that the corroded and uncorroded regions could exist in the same rebar, indicating that the rebar could act as both anode and cathode during the electrochemical process of steel corrosion. Similar fact in relation to the formation of anode and cathode along the perimeter of the same rebar was also reported in the literature (Hansen & Saouma 1999). Moreover, figures 9(a)–(f) illustrate that, at a given time, corrosion initiated regions along the perimeters of B_2 bars are always larger than that of B_1 bars. This observation directly reflects the development of corrosion-induced stresses around the perimeters of rebars. It is widely accepted that the process of rebar corrosion transforms the steel into corrosion products, leading to an expansion in volume that generates stresses in the concrete cover. Figures 9(a)–(f) intuitively ascertain that the maximum stress in concrete cover around B_2 bar would be higher than that around B_1 bar. Furthermore, the region of high-level tensile stress over the surface of B_2 bar would also be much larger than that of B_1 bar. Similar observations in relation to corrosion-induced stresses are also reported in the literature (Xia *et al* 2012).

Furthermore, TCI profiles in figures 9(a)–(f) exhibit that the process of chloride ingress into the porous concrete cover causes localized breakdown of passive protection layer around the circumference of the rebar. The ensuing localized form of corrosion is characterized by a macrocell kind of action between the active steel (anode) and the passive steel (cathode). Circumferential macrocells circulating between the corroded active steel and uncorroded passive steel are formed due to localized corrosion. Therefore, TCI profiles (figures 9(a)–(f)) signify the spatial and temporal evolutions of circumferential macrocells at the surfaces of the rebars. A similar observation in relation to the circumferential macrocell can also found in the literature (Kim & Kim 2008). Owing to the spatial and temporal distribution of TCI values at the surface of a rebar, and to the time-dependent nature of corrosion rate, corrosion penetration depth will also vary along the perimeter of a rebar.

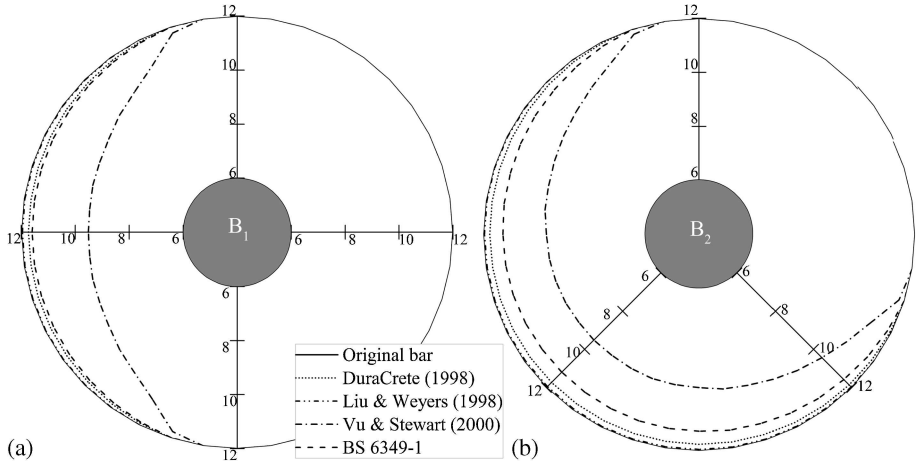

Figure 10. Spatial distribution of corrosion penetration depth along the perimeters of rebars for concrete with $C_c = 25$ mm, $d = 12$ mm and water-to-binder ratio of 0.4 after 10 years: (**a**) B_1 bar and (**b**) B_2 bar.

6.4 *Non-uniform corrosion penetration depth*

Figures 10(a) and (b) show the spatial distribution of corrosion penetration depths along the perimeters of B_1 and B_2 bars, respectively, for the concrete having a cover thickness of 25 mm, a rebar size of 12 mm and a water-to-binder ratio of 0.4 after 10 years from the first onset of corrosion reaction. Perhaps it is important to emphasize here again that both the spatial location and time for the first onset of corrosion reaction are different for B_1 and B_2 bars. Among the values of corrosion penetration depth estimated based on the four corrosion rate empirical models (see figures 10(a) and (b)), those based on the models of Vu & Stewart (2000), and Liu & Weyers (1998) predict higher and lower depths, respectively. While the values of corrosion penetration depth estimated based on the corrosion rate suggested by BS 6349-1 are higher than that estimated based on the corrosion rate model of DuraCrete (1998).

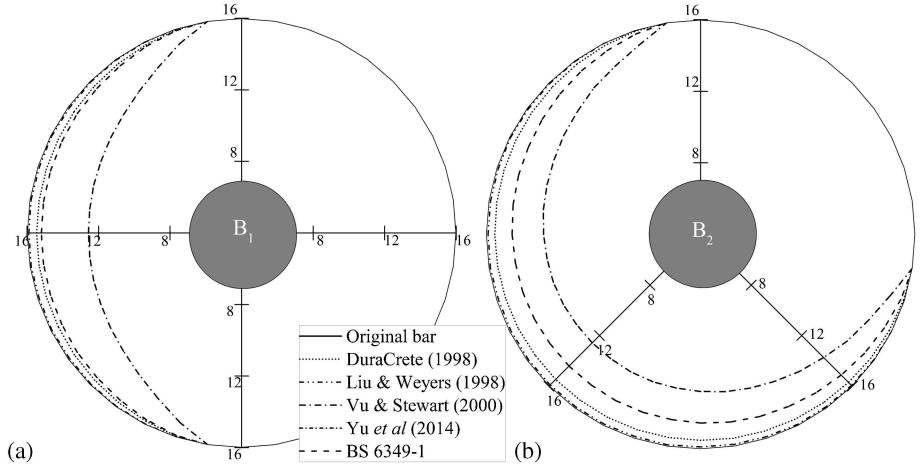

Figure 11. Spatial distribution of corrosion penetration depth along the perimeters of rebars for concrete with $C_c = 40$ mm, $d = 16$ mm and water-to-binder ratio of 0.5 after 20 years: (**a**) B_1 bar and (**b**) B_2 bar.

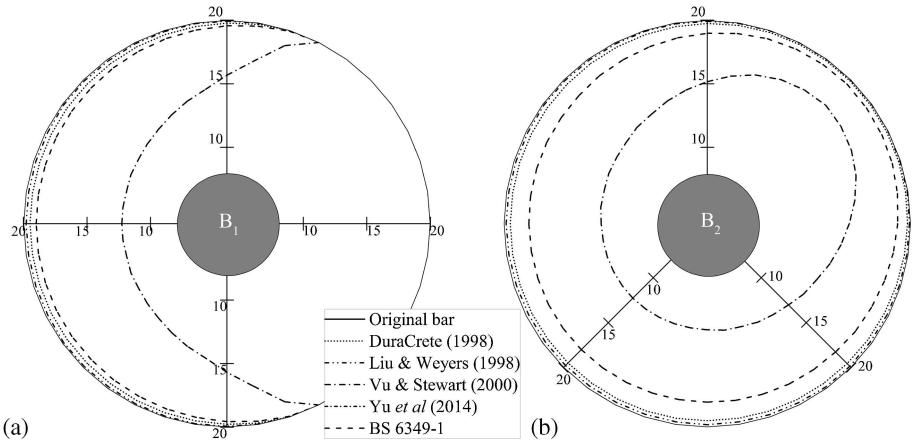

Figure 12. Spatial distribution of corrosion penetration depth along the perimeters of rebars for concrete with $C_c = 30$ mm, $d = 20$ mm and water-to-binder ratio of 0.6 after 25 years: (**a**) B_1 bar and (**b**) B_2 bar.

Figures 11(a) and (b) show the spatial distribution of corrosion penetration depths along the perimeters of B_1 and B_2 bars, respectively, for the concrete having a cover thickness of 40 mm, a rebar size of 16 mm and a water-to-binder ratio of 0.5 after 20 years from the first onset of corrosion reaction. Similar patterns in the spatial distribution of corrosion penetration depths noticed in figures 10(a) and (b) are also observed in figures 11(a) and (b). In addition, figures 11(a) and (b) also include the values of corrosion penetration depth determined based on the corrosion rate model of Yu *et al* (2014). The values of corrosion penetration depth estimated based on the model of Yu *et al* (2014) are even lower than that estimated based on the model of Liu & Weyers (1998) indicating that the corrosion rates predicted by the former are relatively lowest.

Finally, figures 12(a) and (b) show the spatial distribution of corrosion penetration depths along the perimeters of B_1 and B_2 bars, respectively, for the concrete having a cover thickness of 30 mm, a rebar size of 20 mm and a water-to-binder ratio of 0.6 after 25 years from the first onset of corrosion reaction. Similar patterns in the spatial distribution of corrosion penetration depths seen in figures 10 and 11 are also observed in figures 12(a) and (b) Additionally, the corrosion penetration depths have evolved completely along the entire perimeter of B_2 bar (see figure 12(b)).

6.5 *Non-uniform corrosion scenarios*

With respect to the corrosion penetration depth discussed in the preceding sub-section, the following observations are worth emphasizing:

(i) Their spatial distribution along the perimeters of rebars is either complete or incomplete,
(ii) The spatial locations of its maximum value along the perimeter of the rebar are different for a corner bar and a middle bar,
(iii) Its spatial distribution along the perimeter of a corner bar is always longer than that of a middle bar,
(iv) Its spatial distribution along the perimeters of middle and corner bars are non-uniform or uneven.

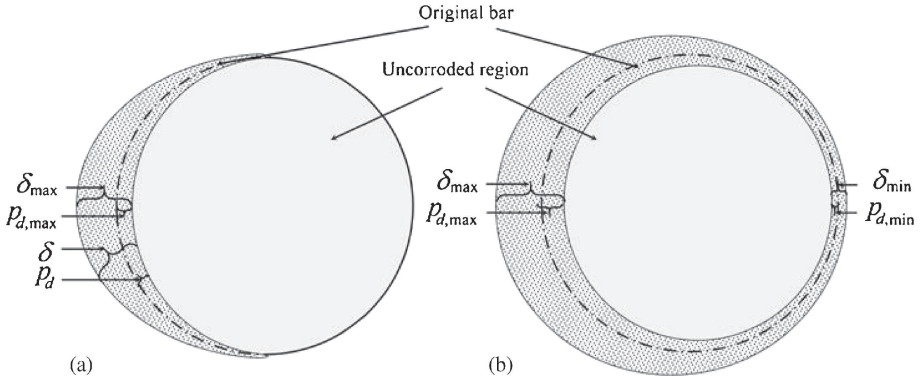

Figure 13. Description of non-uniform scenarios for corrosion penetration depth: (**a**) Scenario I and (**b**) Scenario II.

In the current study, based on the observations drawn from figures 10–12, figures 13(a) and (b) show the two scenarios (I and II) that designate the proposed non-uniform corrosion states. In scenario I (figure 13(a)), the corrosion penetration depth extents only to a portion of the rebar surface as shown in figures 10, 11 and 12(a). Scenario II (figure 13(b)) describes a more severe corrosion, where the corrosion penetration depth spreads over the entire surface of the rebar as shown in figure 12(b). Although, both the corner (i.e. B_2) and middle (i.e. B_1) bars are equally susceptible to corrosion scenarios I and II, the former is more vulnerable to scenario II (e.g. figure 12(b)). Moreover, in figures 13(a) and (b), δ indicates a thick layer of corrosion products that has accumulated at the steel-to-concrete interface during the corrosion propagation phase (i.e. corrosion layer). For the purpose of comparison, the specific volume of the corrosion layer, relative to steel, is assumed to range from 2 to 4 (Zandi *et al* 2013). Furthermore, corrosion scenarios I and II illustrate that the non-uniform corrosion leads to varying p_d and δ along the perimeter of the rebar. These variations have direct impact on the development of non-uniform corrosion induced stresses around the perimeters of rebars. figures 13(a) and (b) are innately linked with the non-uniform corrosion induced stress that varies around the perimeter of the rebar with the change in the thickness of corrosion layer. Thus, the maximum tensile stress would be at the internal concrete surface where the thickness of the corrosion layer is maximum. Similar observations in relation to the non-uniform corrosion-induced stresses around the perimeter of the rebar are also reported in the literature (Xia *et al* 2012).

Qualitative comparisons for scenarios I and II in relation to the non-uniform corrosion layer thickness around steel-concrete interfaces of rebars are presented here. Between the parameters, namely, corrosion layer and corrosion penetration depth, this study choses the former for qualitative comparisons because its thickness can be experimentally measured with high accuracy (e.g. Zhao *et al* 2011a, b). In addition, since relatively large data (both experimental and field) for corrosion layer thickness are available in the literature, this parameter is more suitable for making comparisons. The current discussion also reveals a significant contribution of the proposed numerical framework that it can predict the spatial distribution of corrosion penetration depth, which is very difficult to measure in practice.

The corrosion layer thickness in scenarios I and II is very similar to that observed by Liu & Li (2004) in the corroded samples of rebar obtained from a concrete wall. Moreover, scenario I

closely resembles that noticed by Liu & Li (2004) in rebar samples from a concrete wall exposed to only one side. In addition, scenario I closely compares with the corrosion layer detected by Yuan & Ji (2009) on test specimens degraded under artificial climate environment. Besides, the predicted scenarios I and II are very similar to the patterns of corrosion layer distribution around steel–concrete interfaces of rebars experimentally observed by Zhao *et al* (2011a) and Zhao *et al* (2011b) under laboratory conditions. Furthermore, scenario I closely matches with the spatial distribution of corrosion layer thickness experimentally measured by (Ji *et al* 2012) under laboratory conditions. Finally, the predicted scenario I closely resembles one of the realistic corrosion distribution patterns adopted by (Jang & Oh 2010) for exploring the effects of non-uniform corrosion on the cracking behaviour of concrete cover.

7. Summary and conclusions

The objective of this study is to propose and verify a numerical framework that can efficiently quantify the non-uniform corrosion penetration depth along the perimeter of the rebar in concrete exposed to chloride environment. The corrosion initiation phase is examined through a comprehensive chloride ingress model and the corrosion propagation phase is studied based on a decisive parameter, namely, the corrosion rate.

Numerical solution shows that, in general, TCC build-up along the perimeter of the corner bar (i.e. B_2) is not only faster but also higher than that of the middle bar (i.e. B_1). Moreover, for the given values of cover thickness and water-to-binder ratio, TCI for B_2 bar is faster than that for B_1 bar. In addition, the ratio between TCI of B_1 and B_2 bar is observed to fall within the range of 1.3–1.6, indicating TCI for B_2 bar is 30–60% faster than that for B_1 bar. The larger the rebar, in general, the bigger the obstruction, and therefore, the higher the chloride build-up. The minimum cover thickness required to guarantee a certain number of corrosion-free service life is observed to increase not only with the increase in water-to-binder ratio but also with the rebar locations and sizes. TCI profiles illustrate that, at a given time, corrosion initiated regions along the perimeters of B_2 bars are always larger than that of B_1 bars.

Two scenarios (I and II) that designate non-uniform corrosion states are proposed. In scenario I, the corrosion penetration depth extents only to a portion of the rebar surface, whereas scenario II describes a more severe corrosion, where the corrosion penetration depth spreads over the entire surface of the rebar. Qualitative comparisons of the evaluated non-uniform corrosion states with the variety of available laboratory and field data show good agreement.

In this proposed study, deterministic approach is adopted; however, one of the main intricacies could be the variability and uncertainty contained in the physical parameters involved in the chloride ingress model. Hence, this study needs to be pursued to develop physics based stochastic model of chloride-induced corrosion of reinforcing steel for use in real-life applications. Further, the major area of uncertainly and indeed difficulty remains the quantification of the values for the different parameters used in the model. These can only be resolved by painstaking and ongoing experimental work.

List of symbols

B_c Chloride transfer coefficient at the exposed boundary
B_h Relative humidity transfer coefficient at the exposed boundary
B_T Temperature transfer coefficient at the exposed boundary
c_p Specific heat capacity of concrete/rebar

C_c	Concrete cover thickness
C_{env}	Chloride in the environment
C_f	Free chloride content
C_f^b	Free chloride at the exposed boundary
C_t	Total chloride content
d	Rebar diameter size
D_c	Effective chloride diffusion coefficient
D_c^a	Apparent chloride diffusion coefficient
$D_{c,ref}$	Reference chloride diffusion coefficient
D_h	Relative humidity diffusion coefficient
$D_{h,ref}$	Reference relative humidity diffusion coefficient
D_T	Thermal conductivity of concrete/rebar
h	Relative humidity
h^b	Relative humidity at the exposed boundary
h_{env}	Relative humidity in the environment
i_{corr}	Corrosion rate
p_d	Corrosion penetration depth
t	Time
t	Concrete age
t_e	Exposure time
T	Temperature
T^b	Temperature at the exposed boundary
T_{env}	Temperature in the environment
T_{ref}	Reference temperature
w/b	Water-to-binder ratio
w_e	Evaporable water content
X_c^b	Chloride flux at the exposed boundary
X_h^b	Relative humidity flux at the exposed boundary
X_T^b	Temperature flux at the exposed boundary
ρ	Density of concrete (or) rebar

References

Akiyama M, Frangopol D M and Yoshida I 2010 Time-dependent reliability analysis of existing RC structures in a marine environment using hazard associated with airborne chlorides. *Eng. Struct.* 32(11): 3768–3779

Balabanic G, Bicanic N and Durekovic A 1996 The influence of w/c ratio, concrete cover thickness and degree of water saturation on the corrosion rate of reinforcing steel in concrete. *Cement Concrete Res.* 26(5): 761–769

Baroghel-Bouny V, Thiéry M and Wang X 2011 Modelling of isothermal coupled moisture–ion transport in cementitious materials. *Cement Concrete Res.* 41(8): 828–841

Bastidas-Arteaga E, Chateauneuf A, Sanchez-Silva M, Bressolette P and Schoefs F 2011 A comprehensive probabilistic model of chloride ingress in unsaturated concrete. *Eng. Struct.* 33(3): 720–730

Bazant Z P and Thonguthai W 1978 Pore pressure and drying of concrete at high-temperature. *ASCE J. Eng. Mech.* 104(5): 1059–1079

Bertolini L 2008 Steel corrosion and service life of reinforced concrete structures. *Struct. Infrastruct. Eng.* 4(2): 123–137

Bhargava K, Mori Y and Ghosh A K 2011 Time-dependent reliability of corrosion-affected RC beams – Part 1: Estimation of time-dependent strengths and associated variability. *Nuclear Eng. Des.* 241(5): 1371–1384

BS 6349-1:2000 Maritime structures. Part 1: Code of practice for general criteria. British Standard

Cao C and Cheung M M S 2014 Non-uniform rust expansion for chloride-induced pitting corrosion in RC structures. *Construct. Build. Mater.* 51: 75–81

Detwiler R J, Kjellsen K O and Gjorv O E 1991 Resistance to chloride intrusion of concrete cured at different temperatures. *ACI Mater. J.* 88(1): 19–24

Djerbi A, Bonnet S, Khelidj A and Baroghel-bouny V 2008 Influence of traversing crack on chloride diffusion into concrete. *Cement Concrete Res.* 38(6): 877–883

DuraCrete 1998 Modelling of degradation. DuraCrete-probabilistic performance based durability design of concrete structures. EU-brite EuRam III. Contract BRPR-CT95-0132. Project BE95-1347/R4-5. December. p. 174

Eurocode 3 2005 Design of steel structures – Part 1–2: General rules –Structural fire design, EN 1993–1–2, European committee for standardization, Brussels

Fick A 1855 Ueber diffusion. *Annal. Physik* 170(1): 59–86

Hansen E J and Saouma V E 1999 Numerical simulation of reinforced concrete deterioration: Part II – Steel corrosion and concrete cracking. *ACI Mater. J.* 96(3): 331–338

Iqbal P O and Ishida T 2009 Modeling of chloride transport coupled with enhanced moisture conductivity in concrete exposed to marine environment. *Cement Concrete Res.* 39(4): 329–339

Jang B S and Oh B H 2010 Effects of non-uniform corrosion on the cracking and service life of reinforced concrete structures. *Cement Concrete Res.* 40(9): 1441–1450

Japan Metereological Agency, http://www.data.jma.go.jp/obd/stats/data/en/normal/normal.html (access 27.06.13)

Ji Y S, Zhang B Y, Zhang L L, Ma H R and Zeng P 2012 Propagation of the corrosion layer and model of corrosion distribution on steel re-enforcing bar in concrete. *Zhongguo Kuangye Daxue Xuebao/Journal of China University of Mining and Technology* 41(3): 355–360

JSCE 2007 *Standard specification for concrete structures (Maintenance)*. Tokyo: Society of Civil Engineers

Kim C Y and Kim J K 2008 Numerical analysis of localized steel corrosion in concrete. *Construct. Build. Mater.* 22(6): 1129–1136

Kim K H, Jeon S E, Kim J K and Yang S C 2003 An experimental study on thermal conductivity of concrete. *Cement Concrete Res.* 33(3): 363–371

Kodur V K R and Sultan M A 2003 Effect of temperature on thermal properties of high-strength concrete. *ASCE J. Mater. Civil Eng.* 15(2): 101–107

Kong J S, Ababneh A N, Frangopol D M and Xi Y 2002 Reliability analysis of chloride penetration in saturated concrete. *Probabil. Eng. Mech.* 17(3): 305–315

Kranc S C, Sagues A A and Presuel-Moreno F J 2002 Decreased corrosion initiation time of steel in concrete due to reinforcing bar obstruction of diffusional flow. *ACI Mater. J.* 99(1): 51–53

Li C Q, Melchers R E and Zheng J J 2006 Analytical model for corrosion-induced crack width in reinforced concrete structures. *ACI Struct. J.* 103(4): 479–487

Liu Y P 1996 *Modeling the time-to-corrosion cracking of the cover concrete in chloride contaminated reinforced concrete structures*. Ph.D. Thesis, Blacksburg, Virginia

Liu Y D and Li Y H 2004 Mechanistic model and numerical analysis for corrosion damage of reinforced concrete structure. *Int. J. Fract.* 126(1): 71–78

Liu Y P and Weyers R E 1998 Modeling the time-to-corrosion cracking in chloride contaminated reinforced concrete structures. *ACI Mater. J.* 95(6): 675–681

Marchand J and Samson E 2009 Predicting the service-life of concrete structures – Limitations of simplified models. *Cement Concrete Composites* 31(8): 515–521

Martin-Perez B, Pantazopoulou S J and Thomas M D A 2001 Numerical solution of mass transport equations in concrete structures. *Comput. Struct.* 79(13): 1251–1264

Meira G R, Andrade C, Alonso C, Borba J C and Padilha M 2010 Durability of concrete structures in marine atmosphere zones – The use of chloride deposition rate on the wet candle as an environmental indicator. *Cement Concrete Composites* 32(6): 427–435

Muthulingam S and Rao B N 2014 Non-uniform time-to-corrosion initiation in steel reinforced concrete under chloride environment. *Corros. Sci.* 82: 304–315

Neville A M 1963 *Properties of concrete*, 4th ed, Pearson Education

Oh B H and Jang B S 2003 Chloride diffusion analysis of concrete structures considering effects of reinforcements. *ACI Mater. J.* 100(2): 143–149

Otieno M B, Alexander M G and Beushausen H D 2010 Corrosion in cracked and uncracked concrete – influence of crack width, concrete quality and crack reopening. *Magazine Concrete Res.* 62(6): 393–404

Otieno M, Beushausen H and Alexander M 2012 Prediction of corrosion rate in reinforced concrete structures – A critical review and preliminary results. *Mater. Corrosion* 63(9): 777–790

Papakonstantinou K G and Shinozuka M 2013 Probabilistic model for steel corrosion in reinforced concrete structures of large dimensions considering crack effects. *Eng. Struct.* 57: 306–326

Petcherdchoo A 2013 Time dependent models of apparent diffusion coefficient and surface chloride for chloride transport in fly ash concrete. *Construct. Build. Mater.* 38: 497–507

Pillai S U and Menon D 2009 *Reinforced concrete design*, 3rd ed, Tata McGraw-Hill Education

Raupach M 2006 Models for the propagation phase of reinforcement corrosion – An overview. *Mater. Corrosion* 57(8): 605–613

Rodriguez J, Ortega L M, Casal J and Diez J M 1996 *Corrosion of reinforcement and service life of concrete structures*, Durability of Building Materials and Components 7, Stockholm, 117–126

Saetta A V, Scotta R V and Vitaliani R V 1993 Analysis of chloride diffusion into partially saturated concrete. *ACI Struct. J.* 90(5): 441–451

Samson E and Marchand J 2007 Modeling the effect of temperature on ionic transport in cementitious materials. *Cement Concrete Res.* 37(3): 455–468

Schiessl P and Raupach M 1990 *Influence of concrete composition and microclimate on the critical chloride content in concrete*, Page C L, Treadaway K W J and Bamforth P B (eds) Corrosion of reinforcement in concrete, London (UK), Elsevier Applied Science, 49–58

Shafei B, Alipour A and Shinozuka M 2012 Prediction of corrosion initiation in reinforced concrete members subjected to environmental stressors: A finite-element framework. *Cement Concrete Res.* 42(2): 365–376

Song H W, Lee C H and Ann K Y 2008 Factors influencing chloride transport in concrete structures exposed to marine environments. *Cement Concrete Composites* 30(2): 113–121

Tang L P and Nilsson L O 1993 Chloride binding-capacity and binding isotherms of opc pastes and mortars. *Cement Concrete Res.* 23(2): 247–253

Tuutti K 1982 Corrosion of steel in concrete, Swedish Cement and Concrete Research Institute

Val D V, Chemin L and Stewart M G 2009 Experimental and numerical investigation of corrosion-induced cover cracking in reinforced concrete structures. *ASCE J. Struct. Eng.* 135(4): 376–385

Vu K A T and Stewart M G 2000 Structural reliability of concrete bridges including improved chloride-induced corrosion models. *Struct. Saf.* 22(4): 313–333

Walton J C, Plansky L E and Smith R W 1990 Models for estimation of service life of concrete barriers in low-level radioactive waste disposal, Report prepared for U.S. Nuclear Regulatory Commission, NUREG/CR-5542 EGG-2597

Weyers R E 1998 Service life model for concrete structures in chloride laden environments. *ACI Mater. J.* 95(4): 445–453

Williamson S J and Clark L A 2000 Pressure required to cause cover cracking of concrete due to reinforcement corrosion. *Magazine Concrete Res.* 52: 455–467

Xi Y P, Bazant Z P and Jennings H M 1994 Moisture diffusion in cementitious materials – Adsorption-isotherms. *Adv. Cement Based Mater.* 1(6): 248–257

Xia N, Ren Q W, Liang R Y, Payer J and Patnaik A 2012 Nonuniform corrosion-induced stresses in steel-reinforced concrete. *ASCE J. Eng. Mech.* 138(4): 338–346

Yu B, Yang L, Wu M and Li B 2014 Practical model for predicting corrosion rate of steel reinforcement in concrete structures. *Construct. Build. Mater.* 54: 385–401

Yuan Y S and Ji Y S 2009 Modeling corroded section configuration of steel bar in concrete structure. *Construct. Build. Mater.* 23(6): 2461–2466

Yuan Y, Ji Y and Shah S P 2007 Comparison of two accelerated corrosion techniques for concrete structures. *ACI Struct. J.* 104(3): 344–347

Zandi H K, Lundgren K, Plos M and Coronelli D 2013 Three-dimensional modelling of structural effects of corroding steel reinforcement in concrete. *Struct. Infrastruct. Eng.* 9(7): 702–718

Zhao Y, Hu B, Yu J and Jin W 2011a Non-uniform distribution of rust layer around steel bar in concrete. *Corrosion Sci.* 53(12): 4300–4308

Zhao Y X, Karimi A R, Wong H S, Hu B Y, Buenfeld N R and Jin W L 2011b Comparison of uniform and non-uniform corrosion induced damage in reinforced concrete based on a Gaussian description of the corrosion layer. *Corrosion Sci.* 53(9): 2803–2814